

# Further development of efficient and accurate time integration schemes for meteorological models

Vu Thai Luan,<sup>1\*</sup> Janusz A. Pudykiewicz,<sup>2</sup> Daniel R. Reynolds<sup>1</sup>

<sup>1</sup>Department of Mathematics, Southern Methodist University  
PO Box 750156, Dallas, TX 75275-0156, USA

<sup>2</sup>Meteorological Service of Canada, Recherche en Prévision Numérique 2121  
Trans-Canada Highway, Dorval, Que., Canada H9P IJ3

\* Corresponding author; E-mail: vluan@smu.edu

Co-authors email addresses: Janusz.Pudykiewicz@ec.gc.ca, reynolds@smu.edu

June 24, 2019

## Abstract

In this paper, we investigate the use of higher-order exponential Rosenbrock time integration methods on the shallow water equations on the sphere. This stiff, nonlinear model provides a ‘testing ground’ for accurate and stable time integration methods in weather modeling, serving as the focus for exploration of novel methods for many years. We therefore identify a candidate set of three recent exponential Rosenbrock methods of orders four and five (`exprb42`, `pexprb43` and `exprb53`) for use on this model. Based on their multi-stage structure, we propose a set of modifications to the `phipm/IOM2` algorithm for efficiently calculating the matrix functions  $\varphi_k$ . We then investigate the performance of these methods on a suite of four challenging test problems, comparing them against the `epi3` method investigated previously in [9, 12] on these problems. In all cases, the proposed methods enable accurate solutions at much longer time-steps than `epi3`, proving considerably more efficient as either the desired solution accuracy decreases, or as the test problem nonlinearity increases.

# 1 Introduction

The idea of predicting the weather by solving fluid equations was developed at the end of the nineteenth century, long before the appearance of digital computers. The philosophical basis for the formulation of a forecast problem was deeply rooted in the tradition of analytical mechanics of Lagrange, Laplace and Jacobi. The belief in determinism further influenced the formulation of weather prediction based on the methodology used by Laplace in his analysis of tidal motions.

Despite a strong scientific justification, the meteorological community in the early 1900s never considered the fluid equations as a serious predictive tool because the closed form of a solution was unattainable. This unfavourable reception of a dynamic forecast changed, however, after Richardson published a book on predicting the weather by a numerical process [35]. This seminal contribution contained the first formulation of algorithms for the approximate solution of meteorological equations, leading ultimately to the predictions based on primitive equations which materialized, four decades later, in the mid 1960s.

The widespread use of dynamic models based on the primitive equations led to new theoretical insights including the discovery of chaos by E. Lorenz. The sixties brought to atmospheric sciences the fulfillment of Richardson's dream, as well as the reformulation of the basic work of H. Poincaré on the stability of dynamical systems.

Through the entire process of the development of meteorological models, finding a stable and reasonably efficient time integration scheme has posed a major challenge. In order to describe the scope of these problems, we consider the equations of a geophysical rotating fluid after discretization of the spatial derivatives. The set of meteorological equations can be cast in the form of an autonomous dynamical system

$$\frac{du}{dt} = F(u), \quad u(0) = u_0, \quad (1.1)$$

where  $u \in \mathbb{R}^n$  is the state vector,  $n$  indicates the number of degrees of freedom, and  $F : \mathbb{R}^n \rightarrow \mathbb{R}^n$ .

The eigenvalues of the Jacobian matrix of  $F$  in (1.1) differ by several orders of magnitude, reflecting the fact that the primitive meteorological equations govern processes with time scales ranging from a relatively slow advection to very fast gravity waves. This property is often described as *stiffness* of the equations. The difficult task of solving (1.1) has been a central issue in numerical solution of meteorological models over the past 70 years. At the initial stage of the development of numerical weather prediction models, the time stepping schemes for integration of the primitive meteorological equations were explicit and their convergence was subject to severe restrictions imposed by the Courant Friedrichs Lewy (CFL) stability condition for the gravity waves.

The introduction of semi-implicit methods to meteorological models in the 1970s changed this situation; it became evident that the time step could be increased sixfold

without affecting the overall accuracy [37, 38]. This significant advancement was based on the observation that the right-hand side of (1.1) can be naturally cast in the following semi-linear form

$$\frac{du}{dt} = Lu + N(u), \quad (1.2)$$

where  $L$  and  $N$  are the linear and nonlinear parts, respectively.

The stiffness of (1.1) comes predominantly from the linear part of  $F$ . Consequently, the numerical solution of (1.2) in the semi-implicit approach was performed by approximating the linear term  $Lu$  implicitly, and the nonlinear part  $N(u)$  explicitly. This methodology offers a compromise between the requirements of accuracy and efficiency [39]. Later, Ascher *et. al.* [3] used this idea to develop so-called implicit-explicit methods (IMEX) for time-dependent PDEs. IMEX methods can be considered as modern, more-accurate, semi-implicit methods. They have been widely used in the numerical analysis community, and have shown promising results in the shallow water context [21, 5, 45].

Longer time steps afforded by the semi-implicit scheme liberated significant computing resources which, in turn, were used to include additional physical processes, including calculating the parameterization of clouds, boundary layer processes and radiative transfer. With further increases of the complexity of models and an emerging trend to include smaller scale processes, the semi-implicit scheme was extended to the compressible Euler equations [42]. Subsequent numerical experiments indicated that the semi-implicit scheme could also be applied for the study of convective scale atmospheric motions [40]. The notion of an “ultimate” time stepping method for all meteorological applications was born.

Alternative approaches, based on exponential time integration method, were proposed in recent years. After multiplication of (1.2) by the integrating factor,  $e^{Lt}$ , we obtain the variation-of-constants formula

$$u(t) = e^{Lt}u_0 + \int_0^t e^{(t-\tau)L}N(u(\tau))d\tau. \quad (1.3)$$

Exponential integration schemes based on (1.2)-(1.3) were first considered in the 1960s [7, 25, 33] and later developed by many authors, e.g., Beylkin et al. [4], Cox and Matthews [10], and Hochbruck and Ostermann [16]. For a recent review on exponential integrators, see [18]. Consistent with the fact that the linear part of the problem is solved exactly, exponential integration schemes allow the possibility of very good accuracy and realistic representation of high frequencies, in contrast to semi-implicit schemes. In meteorological applications, Archibald et al. [2] applied the scheme of Beylkin et al. [4], based on the assumption of static splitting expressed by (1.2), to solve the shallow water equations on the sphere.

Clancy and Pudykiewicz [9] applied methods based on a *dynamic linearization* to the shallow water system on an icosahedral geodesic grid [34]. In this approach, equation

(1.1) is linearized at each time step with respect to the continuously changing state of the system,  $u$ . The `phipm` method of Niesen and Wright [32] was used to evaluate exponential functions of the Jacobian operator. Despite the fact that the method allowed long time steps and was very accurate, it was deemed to be too expensive to be of practical importance by some users. This deficiency was addressed in the subsequent paper by Gaudreault and Pudykiewicz [12] who modified the original `phipm` algorithm. They replaced the Arnoldi iteration with the incomplete orthogonalization method introduced by Saad [41]. This strategy followed the idea of using the incomplete orthogonalization method for the time integration of an advection–diffusion equation, suggested by Koskela [22]. The efficiency of the exponential scheme described in [12] was further enhanced by a new method to determine the initial size of the Krylov space based on information from previous time steps.

After introducing optimizations resulting from the application of an incomplete orthogonalization algorithm, an accurate and efficient numerical integration of the shallow water equations, with time steps significantly longer than those in the semi-implicit scheme, became possible. However, at these larger time steps nonlinear effects became more prominent, resulting in reduced accuracy due to its simple approximation of the nonlinear term,  $N(u)$ . This fact pointed to the imminent danger of performing a stable but meaningless integration with a long time step.

The primary purpose of this work is, therefore, to explore time integration schemes that can retain the positive characteristics of the methods outlined in [12], while offering a higher-accuracy approximation of the nonlinearity that remains after dynamic linearization. One of the most promising candidates to fulfill these requirements are the *exponential Rosenbrock methods* [17, 20, 28, 30, 26]. This paper focuses on the use of such methods for solving the meteorological equations, including both additional optimizations to the `phipm` algorithm (which results in a new routine called `phipm_simul_iom2`) for exponential Rosenbrock methods, as well as investigations of their accuracy and efficiency on a range of applicable test problems. This work is especially relevant in the context of the ongoing debate regarding optimal time integration methods for atmospheric models [31].

The paper is organized as follows. The first section provides our rationale for selecting the shallow water equations for a study of efficient time integration methods. Following this, we present a concise description of an autonomous system (1.1) obtained after the spatial discretization of the governing equations on icosahedral grid. We also derive an explicit analytical form of the Jacobian operator. The general formulation of the exponential Rosenbrock schemes, as well as details regarding their implementation, is covered in Sections 3 and 4. The extensive discussion of the results obtained with the new schemes, using the tests reported in [12], is included after the theoretical section. The main objective of this discussion is to demonstrate that the proposed techniques are much more accurate and even more efficient than that the algorithms used in the initial tests reported in [9, 12]. In the last part of the paper, the results are summarized and

future work with the exponential Rosenbrock methods for atmospheric models is outlined.

## 2 Shallow Water Model

The original work with the time integration schemes of Robert [36] was performed using a barotropic model of the Earth's atmosphere. In the years following that seminal contribution, the shallow water equations became a standard tool for the investigation of prototypes of the meteorological models. In this study, we will continue to use a barotropic model to develop more accurate and efficient exponential integration algorithms.

The flow is analyzed on a two-dimensional sphere  $S$  described in Cartesian coordinates by the following parametric equations

$$x = a \cos \theta \cos \phi, \quad y = a \cos \theta \sin \phi, \quad z = a \sin \theta,$$

where  $(\theta, \phi) = (\xi_1, \xi_2)$  are the spherical coordinates,  $\theta$  is the latitude ( $\theta \in [-\pi/2, \pi/2]$ ),  $\phi$  is the longitude ( $\phi \in (0, 2\pi]$ ), and  $a$  is the radius of the sphere. Specifically,  $\theta$  is the angle measured from the  $xy$ - plane, and  $\phi$  is the angle measured in the  $xy$ - plane from the positive  $x$  axis, counterclockwise as viewed from the positive  $z$  axis. At each point of  $S$  we can define the normal vector

$$\mathbf{n} = (\cos \theta \cos \phi, \cos \theta \sin \phi, \sin \theta)^T \quad (2.1)$$

which spans the normal vector space,  $TS^\perp$ .

The tangent space  $TS$  is spanned by two basis vectors

$$\mathbf{e}_1 = \frac{\partial \mathbf{n}}{\partial \theta} = \begin{bmatrix} -\sin \theta \cos \phi \\ -\sin \theta \sin \phi \\ \cos \theta \end{bmatrix}, \quad \mathbf{e}_2 = \frac{\partial \mathbf{n}}{\partial \phi} = \begin{bmatrix} -\cos \theta \sin \phi \\ \cos \theta \cos \phi \\ 0 \end{bmatrix}. \quad (2.2)$$

The Riemannian metric of the sphere with respect to the coordinate system defined by  $(\mathbf{e}_1, \mathbf{e}_2)$  is given by

$$g_{ij} = \left( \frac{\partial x}{\partial \xi_i} \frac{\partial x}{\partial \xi_j} + \frac{\partial y}{\partial \xi_i} \frac{\partial y}{\partial \xi_j} + \frac{\partial z}{\partial \xi_i} \frac{\partial z}{\partial \xi_j} \right) = \begin{bmatrix} a^2 & 0 \\ 0 & a^2 \cos^2 \theta \end{bmatrix}, \quad (2.3)$$

and the inverse of  $(g_{ij})$  is denoted by  $(g^{ij})$ , i.e.  $g_{ij} g^{jk} = \delta_i^k$ .

The equations describing flow of a thin layer of fluid on  $S$  can be cast in the form

$$\frac{\partial \mathbf{u}}{\partial t} = -(\text{Curl}_n \mathbf{u} + f \mathbf{n}) \times \mathbf{u} - \text{grad} \left( \frac{|\mathbf{u}|^2}{2} + g(h + h_s) \right), \quad (2.4)$$

$$\frac{\partial h}{\partial t} + \text{div}(h \mathbf{u}) = 0, \quad (2.5)$$

where  $\mathbf{u}$  is the smooth velocity field on  $S$  with values in  $TS$ ,  $h$  is the smooth scalar field on  $S$  describing the thickness of the fluid layer,  $h_s$  is the height of the surface level ( $h_s \ll a$ ),  $g$  is the gravitational acceleration,  $f = 2\Omega \sin \theta$  is the Coriolis parameter,  $\Omega$  is the angular velocity of the rotation, and  $\times$  denotes the vector product in  $\mathbb{R}^3$ .

After expressing the shallow water equations (2.4)-(2.5) in terms of the Cartesian coordinates [34], followed by integration over the control volumes, and applying the discretization formulae for approximation of the differential operators, we obtain the system of ODEs

$$\begin{aligned}\frac{du_x}{dt} &= -\eta \cdot P_x - G_x \cdot \mathcal{E} \\ \frac{du_y}{dt} &= -\eta \cdot P_y - G_y \cdot \mathcal{E} \\ \frac{du_z}{dt} &= -\eta \cdot P_z - G_z \cdot \mathcal{E} \\ \frac{dh}{dt} &= -D_x \cdot (u_x h) - D_y \cdot (u_y h) - D_z \cdot (u_z h),\end{aligned}\tag{2.6}$$

where  $u_x, u_y, u_z, \mathcal{E} = (u_x^2 + u_y^2 + u_z^2)/2 + g(h + h_s)$ , and  $h$  are the column arrays with Cartesian components of the velocity  $\mathbf{u}$ , total energy and the height field, respectively (all quantities are volume averages over the control volume),  $G_x, G_y, G_z$  are sparse matrices used to evaluate the Cartesian components of the gradient on the sphere, while  $D_x, D_y,$  and  $D_z$  are sparse matrices used to evaluate the divergence  $\text{div}(\mathbf{u}) = D_x \cdot u_x + D_y \cdot u_y + D_z \cdot u_z$ , and  $\eta$  is a column array containing the control volume average values of the absolute vorticity,

$$\eta = \text{Curl}_n \mathbf{u} + f = V_x \cdot u_x + V_y \cdot u_y + V_z \cdot u_z + f.\tag{2.7}$$

Sparse arrays  $V_x, V_y,$  and  $V_z$  are used to calculate the vertical component of the vorticity. For further details consult [34]. The arrays  $P_x, P_y,$  and  $P_z$  contain the Cartesian components of the vector product of the velocity and the surface normal, and have the form

$$\begin{aligned}P_x &= n_y u_z - n_z u_y, \\ P_y &= n_z u_x - n_x u_z, \\ P_z &= n_x u_y - n_y u_x,\end{aligned}$$

where  $n_x, n_y,$  and  $n_z$  are column arrays containing the  $x, y,$  and  $z$  components of the normal vector  $\mathbf{n}$  evaluated at the control volume centers.

A dissipation term of the form  $D_f \cdot \psi$  is added for each prognostic variable  $\psi$  in (2.6). The dissipation operator is the same as that used in the experiments reported in [9],

$$D_f = -\nu \mathcal{L}^2,\tag{2.8}$$

where  $\mathcal{L}$  is a sparse matrix representing the Laplace operator. The dissipation coefficient  $\nu$  in (2.8) is given as

$$\nu = \gamma_h \frac{(\overline{\Delta x})^{n_\gamma}}{\Delta t_e}, \quad (2.9)$$

where  $\gamma_h$  is the coefficient of proportionality,  $n_\gamma = 4$ ,  $\Delta t_e = 240s$ ,

$$\overline{\Delta x} = \sqrt{4\pi a^2/N_g}$$

is the average separation of the node points and  $N_g$  is the number of the nodes in the geodesic grid ( $N_g = 10 \times 2^{2l} + 2$  with  $l$  indicating the grid number).

The system of equations (2.6) can be rewritten in the more compact form of the autonomous system (1.1), with a state vector  $u$  containing the components of the velocity and the height field as

$$u = (u_x^T \ u_y^T \ u_z^T \ h^T)^T. \quad (2.10)$$

The dimension of the state vector  $u$  is thus  $4N_g$ .

The Jacobian  $J$  of the autonomous system (2.6) is a sparse matrix of size  $(4N_g) \times (4N_g)$ , and is given by the formula

$$J = \frac{\partial F}{\partial u}. \quad (2.11)$$

This Jacobian can be written in the symbolic form

$$J = J_v + J_r + J_m, \quad (2.12)$$

where the block array  $J_v$  represents relative vorticity and the block array  $J_r$  accounts for rotation and dissipation. The third block array  $J_m$  represents coupling between the mass field and the velocity field. These block arrays can be written as

$$J_v = - \begin{bmatrix} \{P_x^i V_x^{ij}\} & \{P_x^i V_y^{ij}\} & \{P_x^i V_z^{ij}\} & \{0\} \\ \{P_y^i V_x^{ij}\} & \{P_y^i V_y^{ij}\} & \{P_y^i V_z^{ij}\} & \{0\} \\ \{P_z^i V_x^{ij}\} & \{P_z^i V_y^{ij}\} & \{P_z^i V_z^{ij}\} & \{0\} \\ \{0\} & \{0\} & \{0\} & \{0\} \end{bmatrix}, \quad (2.13)$$

$$J_r = \begin{bmatrix} \{D_f^{ij}\} & \{\eta^i n_z^j \delta^{ij}\} & -\{\eta^i n_y^j \delta^{ij}\} & \{0\} \\ \{\eta^i n_z^j \delta^{ij}\} & \{D_f^{ij}\} & -\{\eta^i n_x^j \delta^{ij}\} & \{0\} \\ \{\eta^i n_y^j \delta^{ij}\} & -\{\eta^i n_x^j \delta^{ij}\} & \{D_f^{ij}\} & \{0\} \\ \{0\} & \{0\} & \{0\} & \{D_f^{ij}\} \end{bmatrix}, \quad (2.14)$$

and

$$J_m = - \begin{bmatrix} \{G_x^{ij} u_x^j\} & \{G_x^{ij} u_y^j\} & \{G_x^{ij} u_z^j\} & \{g G_x^{ij}\} \\ \{G_y^{ij} u_x^j\} & \{G_y^{ij} u_y^j\} & \{G_y^{ij} u_z^j\} & \{g G_y^{ij}\} \\ \{G_z^{ij} u_x^j\} & \{G_z^{ij} u_y^j\} & \{G_z^{ij} u_z^j\} & \{g G_z^{ij}\} \\ \{D_x^{ij} h^j\} & \{D_y^{ij} h^j\} & \{D_z^{ij} h^j\} & \{D_x^{ij} u_x^j + D_y^{ij} u_y^j + D_z^{ij} u_z^j\} \end{bmatrix}, \quad (2.15)$$

where the wave brackets denote matrices (e.g., the expression  $\{P_x^i V_x^{ij}\}$  represents the matrix with  $ij$ -th element equal to  $P_x^i V_x^{ij}$ ).

### 3 Exponential Rosenbrock methods

In this section, we first recall the idea behind exponential Rosenbrock methods and display the stiff order conditions for methods of order up to 5. We then select a set of promising schemes for our numerical experiments of the shallow water equations on the sphere. These include a fourth-order two-stage scheme, a fourth-order parallel stages scheme, and a fifth-order three-stage scheme. Our main references in this section are [17, 20, 28, 30, 26].

#### 3.1 General motivation and ideas

As discussed in the introduction, when integrating the full nonlinear stiff system (1), classical methods like explicit Runge–Kutta are subject to the CFL condition, resulting in unrealistically small time steps. This is mainly because for such systems the Jacobian of the forcing term  $F(u)$  often has a large norm or is even an unbounded operator (causing the stiffness of the system). To overcome this, implicit methods are often used. These standard methods, however, require the solution of nonlinear systems of equations in each step. As this stiffness increases, such methods may require increased computational effort. Alternatively, we consider a class of integrators that can handle the stiffness of this full nonlinear system in an explicit and very accurate way. The idea is first to replace the full nonlinear system (1) by a sequence of semilinear problems (similarly to the idea of deriving Rosenbrock-type methods, see [13, Chap. IV.7]). This can be done by linearizing the flow in each time step around the numerical solution  $u_n$  (due to [33]), leading to

$$u'(t) = F(u(t)) = J_n u(t) + N_n(u(t)), \quad (3.1)$$

where

$$J_n = \frac{\partial F}{\partial u}(u_n) \quad \text{and} \quad N_n(u) = F(u) - J_n u \quad (3.2)$$

are the Jacobian and the nonlinear remainder, respectively. One can then apply exponential Runge–Kutta methods (see [16]) to the semilinear system (3.1); these handle the

stiffness by solving the linear part  $J_n u$  exactly and integrating the nonlinearity  $N_n(u)$  (which is much smaller than the original  $F(u)$ ) in an explicit manner. In this regard, the exact solution at time  $t_{n+1} = t_n + h$  of (3.1) may be represented using the variation-of-constants formula (1.3),

$$u(t_{n+1}) = e^{hJ_n} u(t_n) + \int_0^h e^{(h-\tau)J_n} N_n(u(t_n + \tau)) d\tau. \quad (3.3)$$

This structure provides a recipe for constructing these integrators: the linear part can be integrated exactly by evaluating the action of the matrix exponential  $e^{hJ_n}$  on the vector  $u(t_n)$ , and the integral involving the new nonlinearity  $N_n(u)$  can be approximated by some quadrature. We note that due to the Rosenbrock structure, integration of this nonlinear term can leverage the fact that  $\frac{\partial N_n}{\partial u}(u_n) = \frac{\partial F}{\partial u}(u_n) - J_n = 0$ . This overall procedure results in the so-called *exponential Rosenbrock methods*, see [17, 20]. It is also worth mentioning that other classes of exponential integrators were constructed based on (3.3) as well, see [18].

**Remark 3.1.** In many applications, the forcing term  $F(u)$  naturally has the semilinear form  $F(u(t)) = Lu(t) + N(u(t))$ . Thus stiff semilinear problems of the form (1.2) can be considered as a fixed linearization problem ( $J_n = L$ ). Again, one can approximate its solution by (3.3) as described above, which results in the so-called *explicit exponential Runge–Kutta methods* (see [16]). While these methods do not suffer from the CFL condition for the linear part, the stepsize  $h$  is still limited by the CFL condition due to the nonlinear part. Hence when  $N(u)$  is large, the product of  $h$  and the Lipschitz constant of  $N(u)$  should be sufficiently small to ensure linear stability. In this context, dynamic linearization along the numerical solution offers a potential advantage. This is because in the splitting of the right-hand side,

$$u'(t) = Lu(t) + N(u(t)) = J_n u(t) + N_n(u(t)), \quad (3.4)$$

dynamic linearization constructs  $J_n = A + N'(u_n)$ , leading to a much smaller nonlinearity  $N_n(u)$  that has reduced Lipschitz constant since  $N'_n(u_n) = 0$ . We further note that the new linear part  $J_n u = (A + N'(u_n)) u$  can again be solved exactly. We therefore anticipate that exponential Rosenbrock methods may enable use of even larger time steps than standard explicit exponential Runge–Kutta methods. Moreover, another advantage of exponential Rosenbrock methods is that  $N'_n(u_n) = 0$ , which considerably simplifies the order conditions, and in turn the derivation of higher-order methods.

To illustrate this idea, we present a simple derivation of a second-order scheme.

## 3.2 A second-order scheme and general schemes

The integral in (3.3) is approximated as follows. First, we expand  $u(t_n + \tau)$  in a Taylor series as  $u(t_n + \tau) = u(t_n) + \tau u'(t_n) + \mathcal{O}(\tau^2)$ . We then insert this into  $N_n(u(t_n + \tau))$ , and

perform another Taylor expansion around  $u(t_n)$  (leveraging the fact that  $g'_n(u(t_n)) = 0$ ), to obtain

$$N_n(u(t_n + \tau)) = N_n(u(t_n)) + \mathcal{O}(\tau^2) \quad (3.5)$$

Inserting (3.5) into (3.3) and denoting  $\varphi_1(hJ_n) = \frac{1}{h} \int_0^h e^{(h-\tau)J_n} d\tau$  gives

$$u(t_{n+1}) = e^{hJ_n}u(t_n) + h\varphi_1(hJ_n)N_n(u(t_n)) + \mathcal{O}(h^3). \quad (3.6)$$

Neglecting the local error term  $\mathcal{O}(h^3)$  leads to a second-order scheme, which can be reformulated as

$$u_{n+1} = u_n + h\varphi_1(hJ_n)F(u_n) \quad (3.7)$$

by replacing  $N_n(u(t_n))$  with (3.2) and calculating  $\varphi_1(z) = (e^z - 1)/z$ . Since as  $J_n \rightarrow \mathbf{0}$ , (3.7) approaches the explicit Euler method, it is so-called the *exponential Rosenbrock-Euler method*. We note that this method has been derived before, e.g., [17, 15] that use a different construction. In [9, 43] this method is named EPI2. The present derivation, however, shows directly that this scheme has order of consistency three and thus is a second-order stiffly accurate method. In particular, it is important to emphasize that the error constant behind the Landau notation  $\mathcal{O}$  only depends on the regularity assumptions of  $u(t)$  and  $N_n(u)$  (mentioned at the end of this subsection), but is independent of  $\|J_n\|$ .

To derive higher-order schemes, one must build up higher-order approximations of the integral in (3.3), i.e., with a remainder term of  $\mathcal{O}(h^q)$  ( $q \geq 4$ ). For example, one can approximate  $N_n(u(t_n + \tau))$  by its Taylor expansion of higher-order and plug it into (3.3), which introduces the family of  $\varphi$  functions (similar to  $\varphi_1$ )

$$\varphi_k(hZ) = \frac{1}{h^k} \int_0^h e^{(h-\tau)Z} \tau^{k-1} d\tau, \quad k \geq 1, \quad (3.8)$$

which are bounded (see e.g. [18]) and satisfy the recursion relation

$$\varphi_{k+1}(z) = \frac{\varphi_k(z) - \frac{1}{k!}}{z}, \quad k \geq 1. \quad (3.9)$$

This approach, however, requires the computation of higher derivatives of  $N_n(u)$  which can suffer from instabilities, particularly for schemes of order higher than three, see [23]. Therefore, a preferable solution is to approximate the integral in (3.3) by using a higher-order quadrature rule, yielding

$$u(t_{n+1}) \approx e^{hJ_n}u(t_n) + h \sum_{i=1}^s b_i(hJ_n)N_n(u(t_n + c_i h)) \quad (3.10)$$

with nodes  $c_i$  in  $[0, 1]$  and weights which are matrix functions of  $hJ_n$ , denoted by  $b_i(hJ_n)$  (similarly to the construction of classical Runge–Kutta methods). This introduces a set of unknown intermediate values,  $u(t_n + c_i h)$ , which can again be approximated by using

(3.3) (with  $c_i h$  in place of  $h$ ). To avoid generating new unknowns, another quadrature rule with the same nodes  $c_j$  ( $1 \leq j \leq i-1$  for explicit schemes) and new weights  $a_{ij}(hJ_n)$  is used,

$$u(t_n + c_i h) \approx e^{c_i h J_n} u(t_n) + h_n \sum_{j=1}^{i-1} a_{ij}(hJ_n) N_n(u(t_n + c_j h)). \quad (3.11)$$

As was done for (3.7), we may reformulate (3.10) and (3.11) to obtain the general format of  $s$ -stage explicit exponential Rosenbrock methods

$$U_{ni} = u_n + c_i h \varphi_1(c_i h J_n) F(u_n) + h \sum_{j=2}^{i-1} a_{ij}(hJ_n) D_{nj}, \quad (3.12a)$$

$$u_{n+1} = u_n + h \varphi_1(hJ_n) F(u_n) + h \sum_{i=2}^s b_i(hJ_n) D_{ni} \quad (3.12b)$$

with

$$D_{ni} = N_n(U_{ni}) - N_n(u_n), \quad 2 \leq i \leq s \quad (3.12c)$$

where  $u_n \approx u(t_n)$  and  $U_{ni} \approx u(t_n + c_i h)$  (one can define  $U_{n1} = u_n$  and consequently  $c_1 = 0$  since they do not enter the scheme due to the reformulation, see [30]). Similarly to (3.5), since  $N_n(U_{ni}) - N_n(u_n) = \mathcal{O}(h^2)$  then we have  $D_{ni} = \mathcal{O}(h^2)$  as well. Thus as seen from (3.12), the general methods are small perturbations of the exponential Rosenbrock-Euler method (3.7). By construction, the weights  $a_{ij}(hJ_n)$  and  $b_i(hJ_n)$  are usually linear combinations of the  $\varphi$  functions,  $\varphi_k(c_i h J_n)$  and  $\varphi_k(hJ_n)$ , respectively. Therefore, they are also uniformly bounded independently of  $\|J_n\|$  (i.e. the stiffness). This is a very important feature in comparison to classical exponential schemes (e.g., [10, 43]), where the matrix functions are expanded using *classical* Taylor series expansions (involving powers of the Jacobian, e.g.  $(J_n)^k$ ), that are only valid for nonstiff problems with small  $\|J_n\|$ .

Another significant advantage of exponential Rosenbrock methods (3.12) is that they are fully explicit, and do not require the solution of linear or nonlinear systems of equations.

In general, to analyze the convergence of exponential Rosenbrock methods one needs some regularity assumptions on the solution  $u(t)$  (sufficiently smooth) and  $N_n(u)$  (sufficiently Fréchet differentiable in a neighborhood of the solution), with uniformly bounded derivatives in some Banach space, see [20, 28]

### 3.3 Selected exponential schemes for numerical experiments

As seen above, in order to derive exponential Rosenbrock schemes for stiff problems, one must determine the coefficients  $a_{ij}(hJ_n)$  and  $b_i(hJ_n)$  that guarantee approximation of the nonlinear term to a desired accuracy, even in the presence of large  $\|J_n\|$ . Therefore, a very careful local error analysis must be performed to make sure that the error terms do

not contain powers of  $J_n$ . Recently, Luan and Ostermann [27] derived a new stiff order conditions theory and performed a convergence analysis for methods of arbitrary order. In Table 3.1 we display the required 4 conditions for deriving methods up to order 5, which can be also found in [28]. Note that, for exponential Runge–Kutta methods (applied to a fixed linearization), one needs 16 order conditions for methods up to order 5 (see [29]). This confirms the observation in Remark 3.1 regarding the advantage of using exponential Rosenbrock methods, based on dynamic linearization of the ODE right-hand side.

Table 3.1: Stiff order conditions for exponential Rosenbrock methods up to order 5. Here  $Z, K$  denote arbitrary square matrices and  $\psi_{3,i}(z) = \sum_{k=2}^{i-1} a_{ik}(z) \frac{c_k^2}{2!} - c_i^3 \varphi_3(c_i z)$ .

No.	Order condition	Order
1	$\sum_{i=2}^s b_i(Z) c_i^2 = 2\varphi_3(Z)$	3
2	$\sum_{i=2}^s b_i(Z) c_i^3 = 6\varphi_4(Z)$	4
3	$\sum_{i=2}^s b_i(Z) c_i^4 = 24\varphi_5(Z)$	5
4	$\sum_{i=2}^s b_i(Z) c_i K \psi_{3,i}(Z) = 0$	5

With these stiff order conditions in hand, one can easily derive numerous methods of order up to 5. For practical implementation, however, one must optimize the coefficients and stages for improved accuracy and computational efficiency. Guided by this, we select the following three representative schemes for our applications.

First, we consider a fourth-order scheme satisfying the stiff order conditions, named `exprb42` in [26]:

$$U_{n2} = u_n + \frac{3}{4}h\varphi_1\left(\frac{3}{4}hJ_n\right)F(u_n), \quad (3.13a)$$

$$u_{n+1} = u_n + h\varphi_1(hJ_n)F(u_n) + h\frac{32}{9}\varphi_3(hJ_n)(N_n(U_{n2}) - N_n(u_n)). \quad (3.13b)$$

We note that this uses only two stages, and is therefore considered as a superconvergent scheme.

Second, we consider a fourth-order 3-stage scheme satisfying the stiff order conditions, named `pexprb43` in [30]:

$$U_{n2} = u_n + \frac{1}{2}h\varphi_1\left(\frac{1}{2}hJ_n\right)F(u_n), \quad (3.14a)$$

$$U_{n3} = u_n + h\varphi_1(hJ_n)F(u_n), \quad (3.14b)$$

$$u_{n+1} = u_n + h\varphi_1(hJ_n)F(u_n) + h\varphi_3(hJ_n)(16D_{n2} - 2D_{n3}) + h\varphi_4(hJ_n)(-48D_{n2} + 12D_{n3}). \quad (3.14c)$$

We note that since  $U_{n3}$  does not depend on  $U_{n2}$  these two stages may be computed in parallel (hence the “p” preceding the name).

Third, we consider a fifth-order scheme satisfying the stiff order conditions, named `exprb53` in [28]:

$$U_{n2} = u_n + \frac{1}{2}h\varphi_1\left(\frac{1}{2}hJ_n\right)F(u_n), \quad (3.15a)$$

$$U_{n3} = u_n + \frac{9}{10}h\varphi_1\left(\frac{9}{10}hJ_n\right)F(u_n) + h\frac{27}{25}\varphi_3\left(\frac{1}{2}hJ_n\right)D_{n2} + h\frac{729}{125}\varphi_3\left(\frac{9}{10}hJ_n\right)D_{n2}, \quad (3.15b)$$

$$u_{n+1} = u_n + h\varphi_1(hJ_n)F(u_n) + h\varphi_3(hJ_n)(18D_{n2} - \frac{250}{81}D_{n3}) + h\varphi_4(hJ_n)(-60D_{n2} + \frac{500}{27}D_{n3}), \quad (3.15c)$$

We note that this is also superconvergent, as it uses only three stages.

We further note that the vectors  $D_{n2}$  and  $D_{n3}$  in the methods `pexprb43` and `exprb53` are given by (3.12c), i.e.,  $D_{n2} = N_n(U_{n2}) - N_n(u_n)$ ,  $D_{n3} = N_n(U_{n3}) - N_n(u_n)$ .

For comparison purposes, we also include the third-order exponential multistep scheme named `epi3`, proposed in [43]:

$$u_{n+1} = u_n + h\varphi_1(hJ_n)F(u_n) + h\frac{2}{3}\varphi_2(hJ_n)R_{n-1}, \quad (3.16)$$

where  $R_{n-1} = F(u_{n-1}) - F(u_n) - J_n(u_{n-1} - u_n)$ . This scheme is a classical method as it does not satisfy the *stiff* order conditions for exponential multistep methods of order 3 (see [19]), i.e., the error terms contain powers of  $J_n$ . Given the initial value  $u_0$ , this method requires the computation of the additional starting value  $u_1$ . For the numerical results in Section 5, we compute this additional initial condition using a single step of the exponential Rosenbrock-Euler method (3.7); as the local error of this method matches the  $\mathcal{O}(h^3)$  global error of (3.16), it provides a suitable method for generation of this missing initial condition. We finally note that this method was previously used in [9, 12] for the simulation of the shallow water model on the sphere, and so inclusion of this method in our tests allows direct comparison with the methods tested in those earlier works.

## 4 Implementation of exponential integrators

In this section, we briefly review some state-of-the-art algorithms for the implementation of exponential integrators. We then discuss our modifications to one of these algorithms to enhance efficiency for our proposed exponential Rosenbrock methods. Finally, we discuss specific details in using our new algorithm for the three selected exponential Rosenbrock methods `exprb42`, `pexprb43`, and `exprb53`.

### 4.1 The state-of-the-art algorithms

The implementation of exponential integrators requires computing the action of matrix functions  $\varphi_k(hJ_n)$  on vectors  $v_k$ . In 1997, Hochbruck and Lubich [14] analyzed Krylov subspace methods for efficiently computing the action of a matrix exponential (with large

norm) on some vector. Since then, there have been dramatic advances in constructing more efficient techniques, even for the evaluation of a linear combinations of  $\varphi$ -functions acting on sets of vectors  $v_0, \dots, v_p$ ,

$$\varphi_0(A)v_0 + \varphi_1(A)v_1 + \varphi_2(A)v_2 + \dots + \varphi_p(A)v_p, \quad (4.1)$$

which is crucial within calculations of each stage in exponential schemes. In particular, we highlight a number of state-of-the-art algorithms. `expmv`, proposed by Al-Mohy and Higham in [1], uses a truncated standard Taylor series expansion. `phipm` was proposed by Niessen and Wright in [32], and uses adaptive Krylov subspace methods. Finally, `expleja` was proposed by Caliari *et al.* in [6], and uses Leja interpolation. Among these, it turns out that `phipm` offers an advantage in terms of computational time. This algorithm is developed based on an adaptive time-stepping method to evaluate (4.1) using only one matrix function,  $\varphi_p(\tau_k A)w_p$ , in each substep, where  $w_p$  is a vector resulting from the time-stepping method, and  $\tau_k \leq 1$  is a substep size. This can be carried out in a lower dimensional Krylov subspace (with one Krylov projection needed). When computing this matrix function, standard Krylov subspace projection methods are employed, i.e., using the Gram-Schmidt orthogonalization procedure (the Arnoldi iteration). For improved accuracy and efficiency, the dimension of these Krylov subspaces and the number of substeps  $\tau_k$  are chosen adaptively. More recently, the `phipm` routine was modified by Gaudreault and Pudykiewicz in [12] to use the incomplete orthogonalization method (IOM) within the Arnoldi iteration. They additionally adjusted the two crucial initial parameters for starting the Krylov adaptivity in order to further reduce the computational time. Their result is a new routine named `phipm/IOM2`. It is shown in [12] that this algorithm offers a significant computational advantage compared to `phipm` for integrating the shallow water equations on the sphere.

## 4.2 The time-stepping technique for computing a linear combination of $\varphi$ -functions

In order to contextualize the further improvements that we have made to `phipm/IOM2` described in Section 4.3, we describe the idea of the adaptive time-stepping method (see [32]) for evaluating the linear combination (4.1) efficiently.

The linear combination (4.1) is precisely equal to the solution  $u(1)$  of the ODE

$$u'(t) = Au(t) + v_1 + tv_2 + \dots + \frac{t^{p-1}}{(p-1)!}v_p, \quad u(0) = v_0. \quad (4.2)$$

The time-stepping technique leverages this equivalence to approximate  $u(1)$  by discretizing  $[0, 1]$  into subintervals  $0 = t_0 < t_1 < \dots < t_K = 1$ , having widths  $\tau_k = t_{k+1} - t_k$ . Then by exploiting the relation between  $u(t_{k+1})$  and  $u(t_k)$ , we have

$$u(t_{k+1}) = \varphi_0(\tau_k A)u(t_k) + \sum_{i=1}^p \tau_k^i \varphi_i(\tau_k A) \sum_{j=0}^{p-i} \frac{t_k^j}{j!} v_{i+j}. \quad (4.3)$$

With the help of the recursion relation (3.9), (4.3) may be simplified to

$$u(t_{k+1}) = \tau_k^p \varphi_p(\tau_k A) w_p + \sum_{j=0}^{p-i} \frac{t_k^j}{j!} w_j, \quad (4.4)$$

where the vectors  $w_j$  satisfy another recurrence relation,

$$w_0 = u(t_k), \quad w_j = Aw_{j-1} + \sum_{\ell=0}^{p-j} \frac{t_k^\ell}{\ell!} v_{j+\ell}, \quad j = 1, \dots, p. \quad (4.5)$$

This interesting result implies that evaluating the linear combination (4.1) (i.e.  $u(t_K) = u(1)$ ), which typically consists of  $(p + 1)$  matrix-vector multiplications, can be accomplished instead by using only one matrix function  $\varphi_p(\tau_k A) w_p$  in each substep. Since  $0 < \tau_k \leq 1$ , this task can be carried out in a lower dimensional Krylov subspace, and only one Krylov projection is needed. Therefore, this approach may reduce the computational cost significantly in comparison with a standard Krylov algorithm. More specifically, it is known that constructing a Krylov subspace of dimension  $m$  for approximating  $\varphi_p(A)v$  requires a total computational cost of  $\mathcal{O}(m^2)$ . The time-stepping method (4.4)-(4.5), replaces this by  $K$  (not too large) Krylov projections (corresponding to  $\varphi_p(\tau_k A) w_p$ ), performed in smaller Krylov subspaces of dimension  $m_1, \dots, m_K < m$ , which require a total computational cost of  $\mathcal{O}(m_1^2) + \dots + \mathcal{O}(m_K^2)$ . This overall cost is expected to be less than  $\mathcal{O}(m^2)$ . This might be not true if  $K$  is too large, e.g. the case when the spectrum of  $A$  is very large. This situation, however, is handed by using the adaptive Krylov algorithm developed in [32], which allows adaptivity of both the dimension  $m$  and the step sizes  $\tau_k$ .

### 4.3 A modification of the `phipm/IOM2` routine

Due to the multi-stage structure of exponential Rosenbrock methods, we have modified the implementation slightly from that used for the `epi3` method in [9, 12]. The details of the previous version (`phipm/IOM2`) have been previously described in [12] (Algorithm 2), which we do not reproduce here, except for the features relating to our Rosenbrock-specific modifications. In particular, each time step of the `epi3` method requires evaluation of the linear combination (4.1); we note that in this formula each of the  $\varphi_k$  functions is evaluated at the same argument  $A$ , and multiplied by a distinct vector  $v_k$ . Moreover, this method utilizes substepping in time based on formula (4.4), that effectively evaluates the  $\varphi_k$  functions at fractions of the argument,  $\tau_k A$ , where  $0 < \tau_k \leq 1$ . Finally, `phipm/IOM2` leverages the recurrence relation (4.5) so that each substep relies on a set of matrix-vector products,  $Aw_{j-1}$ .

We now revisit the structure of the multi-stage exponential Rosenbrock methods from Section 3.3. Unlike equation (4.1), these methods compute stages  $U_{n,j}$  and time-evolved

solutions  $u_{n+1}$  by evaluating the  $\varphi$  functions at fractions of the matrix  $A$ :

$$w_k = \sum_{l=0}^p \varphi_l(c_k A)v_l, \quad k = 2, \dots, N_s, \quad (4.6)$$

where now the values  $c_2, \dots, c_{N_s}$  denote an array of “time” scaling factors used for each  $v_k$  output. We further note that the proposed methods only utilize a subset of the  $\varphi_l$  functions (e.g., `exprb53` uses only  $\varphi_1, \varphi_3$  and  $\varphi_4$ ); equivalently, multiple vectors  $v_l$  in equation (4.6) will be zero.

Due to these structural differences between multi-stage and multi-step exponential methods, our new `hipm_simul_iom2` function incorporates two specific changes from the `hipm/IOM2` function used in [12].

First, we simultaneously compute all of the  $w_k$  outputs in equation (4.6), instead of computing these one at a time. This is accomplished by first requiring that the entire array  $c_2, \dots, c_{N_s}$  be input to the function. We then ensure that within the substepping process (4.4), these  $c_j$  values align with a subset of the internal substep times  $t_k$ ; at each of these moments the solution vector is stored, and on output the full set  $\{w_k\}_{k=1}^{N_s}$  is returned. We note that this idea is not new, as it is similar to an approach used in [44]; ours differs in that we explicitly stop at each  $c_k$  instead of computing the  $w_k$  vectors through interpolation, thereby guaranteeing no loss of solution accuracy.

Second, we leverage the fact that some of the input vectors  $v_l$  are identically zero, so within the recursion (4.5) we check whether  $w_{j-1} \neq 0$  before computing the matrix-vector product  $A w_{j-1}$ . As matrix-vector products require  $\mathcal{O}(N^2)$  work, while verification that  $u \neq 0$  requires only  $\mathcal{O}(N)$ , this can result in significant savings for large  $N$ , especially when a significant fraction of these products involve vectors  $w_{j-1} = 0$ .

Aside from these changes, all components of `hipm/IOM2` are directly retained, including the strategy for adapting the substep size and Krylov subspace size.

#### 4.4 Details of implementation of `exprb42`, `pexprb43` and `exprb53`

We now make use of `hipm_simul_iom2` for implementing the three selected exponential Rosenbrock schemes `exprb42`, `pexprb43` and `exprb53`. In the following we will denote  $A = hJ_n$  and  $v = hF(u_n)$  for simplicity.

*Implementation of `exprb42`:* In view of the structure of `exprb42` given in (3.13), it requires two calls to `hipm_simul_iom2`:

- (i) Evaluate  $y_1 = \varphi_1(\frac{3}{4}A)w_1$  with  $w_0 = 0$  and  $w_1 = \frac{3}{4}v$  to get  $U_{n2} = u_n + y_1$ .
- (ii) Evaluate  $w = \varphi_1(A)v_1 + \varphi_3(A)v_3$  with  $v_0 = v_2 = 0$ ,  $v_1 = v$  and  $v_3 = \frac{32}{9}hD_{n2}$  to get  $u_{n+1} = u_n + w$ .

*Implementation of pexprb43:* Due to the structure of `pexprb43` given in (3.14), we only need two calls to `phipm_simul_iom2`:

- (i) Evaluate both  $y_1 = \varphi_1(\frac{1}{2}A)v$  and  $z_1 = \varphi_1(A)v$  simultaneously to compute the stages  $U_{n2} = u_n + \frac{1}{2}y_1$  and  $U_{n3} = u_n + z_1$ .
- (ii) Evaluate  $w = \varphi_3(A)v_3 + \varphi_4(A)v_4$  with  $v_0 = v_1 = v_2 = 0$ ,  $v_3 = h(16D_{n2} - 2D_{n3})$  and  $v_4 = h(-48D_{n2} + 12D_{n3})$  to get  $u_{n+1} = U_{n3} + w$ .

*Implementation of exprb53:* Although `exprb53` is a 3-stage scheme like `pexprb43`, its structure (3.15) is more complicated since the  $\varphi$ -functions in the stage  $U_{n3}$  involve different fractions of  $A$ . This requires one additional call to `phipm_simul_iom2` as compared to `pexprb43`:

- (i) Evaluate both  $y_1 = \varphi_1(\frac{1}{2}A)v$  and  $z_1 = \varphi_1(\frac{9}{10}A)v$  simultaneously to get  $U_{n2} = u_n + \frac{1}{2}y_1$ .
- (ii) Evaluate both  $y_3 = \varphi_3(\frac{1}{2}A)w_3$  and  $z_3 = \varphi_3(\frac{9}{10}A)w_3$  simultaneously with  $w_3 = hD_{n2}$  to get  $U_{n3} = u_n + \frac{9}{10}z_1 + \frac{27}{25}y_3 + \frac{725}{125}z_3$ .
- (iii) Evaluate  $w = \varphi_1(A)v_1 + \varphi_3(A)v_3 + \varphi_4(A)v_4$  with  $v_0 = v_2 = 0$ ,  $v_1 = v$ ,  $v_3 = h(18D_{n2} - \frac{250}{81}D_{n3})$  and  $v_4 = h(-60D_{n2} + \frac{500}{27}D_{n3})$  to get  $u_{n+1} = u_n + w$ .

## 5 Numerical experiments

In the following subsections we compare the performance of the proposed set of exponential integration methods against the `epi3` method previously examined in [9, 12]. As in those papers, we focus on a set of standard test problems, originally introduced by Williamson et al. [46]. These test problems are ordered in increasing difficulty: the Lauter test (with analytical solution) is presented in Section 5.1, the Rossby-Haurvitz wave test is presented in Section 5.2, the isolated mountain test is presented in Section 5.3, and the unstable jet test is presented in Section 5.4. As with the studies [9, 12], we performed these experiments with the shallow water equations on an icosahedral grid. The state vector for each test problem consisted of four prognostic variables, defined over grid number 6 with  $N_g = 40,962$  vertices, amounting to a total of 163,848 unknowns. All simulations were run in serial in MATLAB using SMU’s *Maneframe2* cluster, where each node is comprised of dual Intel Xeon E5-2695v4 2.1 GHz 18-core “Broadwell” processors with 256 GB of DDR4-2400 memory.

For each test problem, we compare the `epi3`, `exprb42`, `pexprb43` and `exprb53` methods discussed in Section 3. We use the `phipm/IOM2` method for `epi3` and all other methods use the `phipm_simul_iom2` method, as these proved the most efficient for each of the respective methods. Both the `phipm/IOM2` and `phipm_simul_iom2` methods were run using

a tolerance of  $10^{-4}$ , an initial Krylov subspace of size 1 (this is adapted automatically throughout each run), and an incomplete orthogonalization length of 2.

The parameter  $\gamma_h$  used in the dissipation coefficient (2.9) in these experiments was set to  $0.04 \times 10^{-2}$  for all tests except for the unstable jet test in Section 5.4, where this was increased to  $1.25 \times 10^{-2}$ .

For each test, we present a variety of data to examine the performance of the proposed exponential integration methods on each problem. As both the accuracy and the work required per time step for each method differ, with higher-order methods generally requiring more work per step, simple measurements of CPU time or error for the same time step sizes cannot accurately capture the full “performance” picture. Hence, for each test problem we initially provide convergence plots showing the error in the height field as a function of time step size. Here, we examine only the relative  $l_\infty$  solution error in the spatial solution at each time since results in [12] showed that these were essentially equivalent to errors computed in the  $l_1$  and  $l_2$  norms. Then using these results, we selected specific time step sizes that provided similar levels of accuracy ( $10^{-4}$ ,  $10^{-5}$ ,  $10^{-6}$  and  $10^{-7}$ ) for each method on each problem, where in general the higher-order methods could use larger step sizes than lower-order methods. Finally, using these method-specific step sizes, we present fair comparisons of the efficiency (error vs CPU time) of each method on each test problem.

The most important conclusion from the experiments in this section is somewhat unsurprising: when increased accuracy is desired, the higher-order methods are much more efficient than the lower-order methods. However, when less accuracy is desired, the lower-order methods are competitive. In addition to this conclusion, we find that even at these larger step sizes the proposed methods exhibit similar conservation properties, and obtain high-quality solutions, in comparison with the `epi3` method (and hence with the EPI2, explicit RK4 and semi-implicit predictor-corrector methods examined in [9, 12, 8]).

## 5.1 Time dependent zonal flow

We begin with a test problem that affords an analytical solution: the Lauter test of time dependent zonal flow [34, 24], using the parameters  $u_0 = 2\pi a/12$  m/day,  $k_1 = 133681$  m<sup>2</sup>/s<sup>2</sup>,  $k_2 = 10$  m<sup>2</sup>/s<sup>2</sup>, and  $\alpha = \pi/4$ . In Figure 5.1 we show two plots. On the left we present a standard convergence plot showing error after 1 simulated day as a function of time step size; on the right we fix each method’s step size to 2 hours, and plot the accumulated solution error over a 10 day simulation. We note that all curves in the convergence plot “bottom out” at an error floor of approximately  $10^{-5}$  – this corresponds to the accuracy of the spatial grid used in these tests. We further note that the error history plot shows identical results for `epi3` as in [12], and that the accumulated error of the proposed methods is uniformly lower than that of `epi3`.

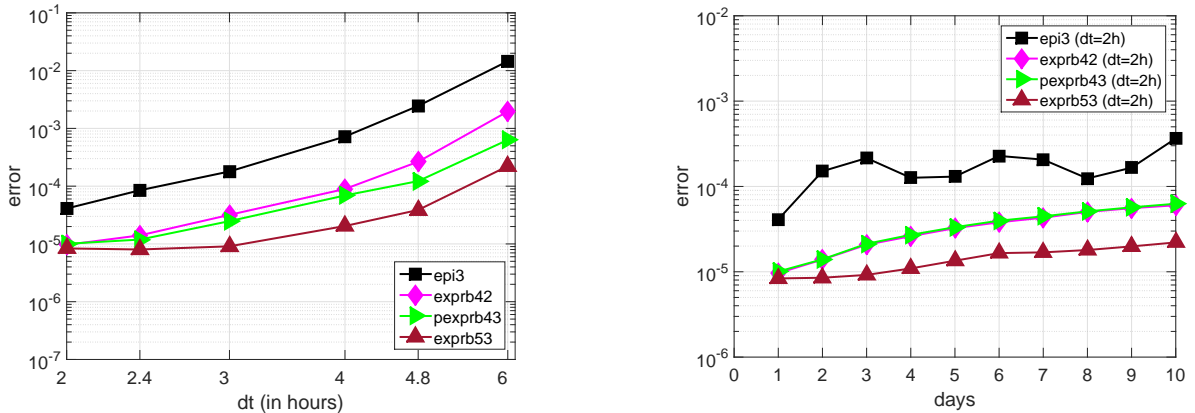


Figure 5.1: Error measures for the height field in the Läuter test: error after one simulated day using various time step sizes (left), and time history of errors over 10 simulated days using a 2 hour time-step for each method (right).

## 5.2 Rossby-Haurvitz waves

The shallow water equations used in this study admit several forms of waves including gravity, Poincaré (or inertio-gravity), Kelvin, and Rossby waves. In this section we investigate the latter of these, motivated by their role in our understanding of atmospheric circulation. Furthermore, the Rossby wave number four, used here, is stable as indicated by analytical studies. The investigation whether or not our time integration schemes can maintain this stability is of crucial importance.

As in [12], we present a wide range of results for the Rossby-Haurvitz wave simulation. These are grouped into two categories: results concerned with solution error, and results associated with conservation. When computing solution error in this problem, we compare against a high-accuracy reference solution in the absence of an analytical solution. This reference solution is computed using the `pexprb43` method with a small time step size of 30 seconds. We then compute the  $l_\infty$  error in the height field by comparing other solutions against this reference.

In Figure 5.2 we present two standard “log-log” convergence plots, showing solution error vs time step size, for each method; on the left we compute errors after one simulated day and on the right after 10 simulated days. Both plots tell the same story: when using the same step size the higher-order methods obtain much smaller solution error, or equivalently, higher-order methods can attain a desired solution error with much larger time step sizes.

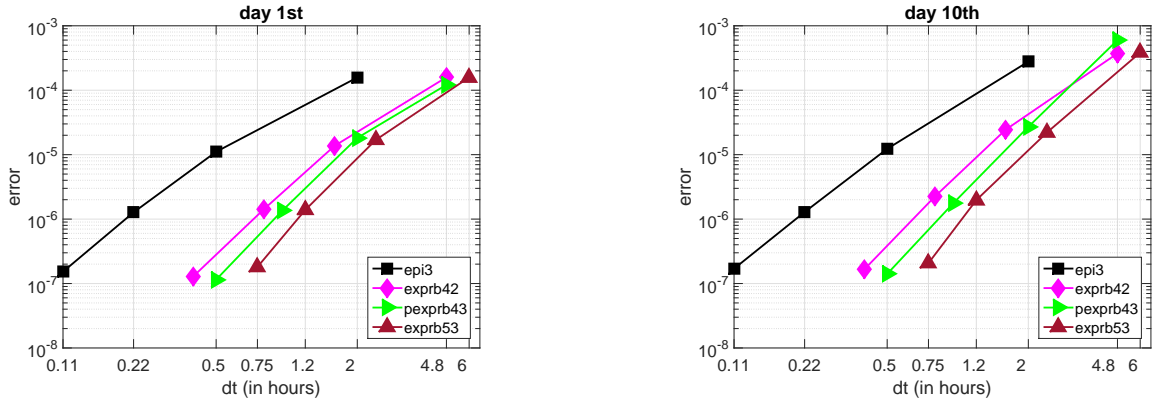


Figure 5.2: Convergence plots for the Rossby-Haurwitz test. We plot  $l_\infty$  error in the height field as a function of time step size after 1 simulated day (left) and after 10 simulated days (right).

Based on these results, we selected a set of time step sizes for each method so that it could obtain accuracies approximately equal to  $10^{-4}$ ,  $10^{-5}$ ,  $10^{-6}$  and  $10^{-7}$  after one simulated day. These values are shown in the following Table 5.1. Of particular interest is that the ratio of time step sizes between `epi3` and the proposed methods increase precipitously as both the accuracy requirements become more stringent, and as the method order increases, indicating promise for higher-order methods when increased accuracy is needed. The smallest ratio of 2.4 occurs in the `exprb42` and `pexprb43` methods at accuracy of  $10^{-4}$ , and the largest ratio of 6.75 occurs in the `exprb53` method at an accuracy of  $10^{-7}$ .

Table 5.1: The time step sizes in seconds used for each method to obtain desired accuracies after one simulated day on the Rossby-Haurwitz wave test. In parenthesis, we include the normalized step sizes as compared with `epi3` (i.e., we divide by the `epi3` step size at each accuracy).

Method	Accuracy			
	$10^{-4}$	$10^{-5}$	$10^{-6}$	$10^{-7}$
<code>epi3</code>	7200	1800	800	400
<code>exprb42</code>	17280 (2.4)	5760 (3.2)	2880 (3.6)	1440 (3.6)
<code>pexprb43</code>	17280 (2.4)	7200 (4)	3456 (4.32)	1800 (4.5)
<code>exprb53</code>	21600 (3)	8640 (4)	4320 (5.4)	2700 (6.75)

Using these step sizes, in Figure 5.3 we plot the efficiency (error vs CPU time) for each method at both one and ten simulated days. While qualitatively similar, these plots connote an expected story: when low-accuracy simulations are desired the low-order `epi3` method is the most efficient, whereas for accuracies of  $\sim 10^{-5}$  or tighter the proposed

higher-order methods are more efficient. We further note that for this test problem, the increased work-per-step required for the fifth-order `exprb53` method renders it non-competitive for any of the accuracy levels examined; however these results imply that it would become the most efficient method for accuracies tighter than  $\sim 10^{-8}$ . We note that this data is also plotted logarithmically, indicating that once the higher-order methods overtake `epi3`, their efficiency benefit over `epi3` improves dramatically.

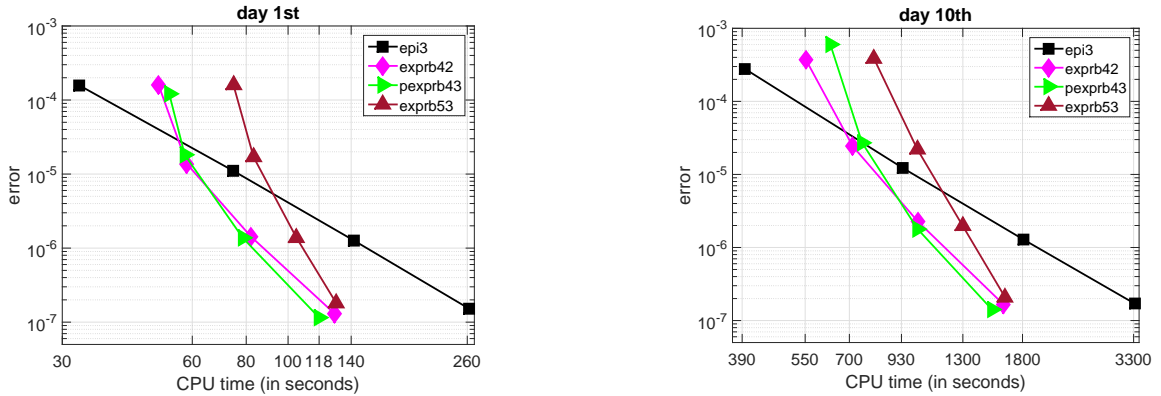


Figure 5.3: Efficiency plots for the Rossby-Haurwitz test. We plot the  $l_\infty$  error in the height field as a function of CPU time for a variety of time step sizes. On the left we plot results after one simulated day, on the right after 10 simulated days.

Also using the time step sizes from Table 5.1, in Figure 5.4 we plot the time history of the computed error in each method over fifteen simulated days. While this plot includes a large amount of data, the salient result is that for each choice of time step size, all methods exhibit numerical stability over the full 15 day duration, with errors that do not accumulate dramatically throughout the simulation.

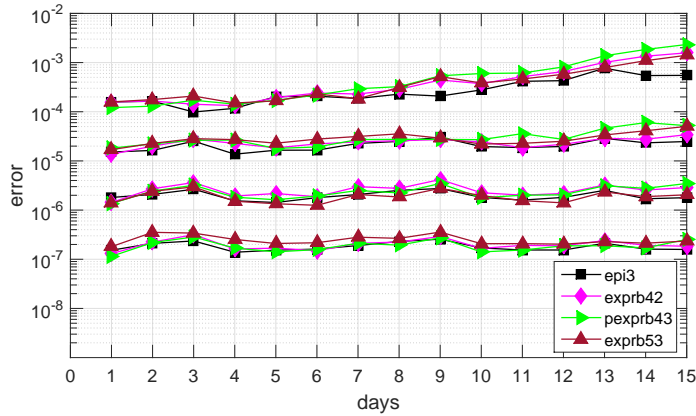


Figure 5.4: Time history of error for the Rossby-Haurwitz test. We plot the  $l_\infty$  error in the height field over 15 simulated days, using a variety of time step sizes.

The following Table 5.2 quantifies these results in slightly more detail. Specifically, it shows the ratio in CPU times required for the `epi3` method in comparison with the proposed methods, for each of the desired accuracies in performing one simulated day of the Rossby-Haurwitz wave test. As described earlier, for a desired accuracy of  $10^{-4}$  the `epi3` method takes less time than all of the higher-order methods (from 44% to 65%); however for tighter tolerances the higher-order methods are generally faster (with the exception being `exprb53` at  $10^{-5}$ ). For the tightest investigated tolerance of  $10^{-7}$ , each of the proposed methods were over twice as fast as `epi3`, with `pexprb43` attaining the greatest efficiency improvement.

Table 5.2: Speedup factor for the proposed methods in comparison with `epi3` for one simulated day of the Rossby-Haurwitz test. Time steps are chosen according to Table 5.1.

Speedup	Accuracy			
	$10^{-4}$	$10^{-5}$	$10^{-6}$	$10^{-7}$
$\text{cpu}_{\text{epi3}}/\text{cpu}_{\text{exprb42}}$	0.65	1.28	1.73	2.04
$\text{cpu}_{\text{epi3}}/\text{cpu}_{\text{pexprb43}}$	0.62	1.29	1.80	2.22
$\text{cpu}_{\text{epi3}}/\text{cpu}_{\text{exprb53}}$	0.44	0.90	1.36	2.02

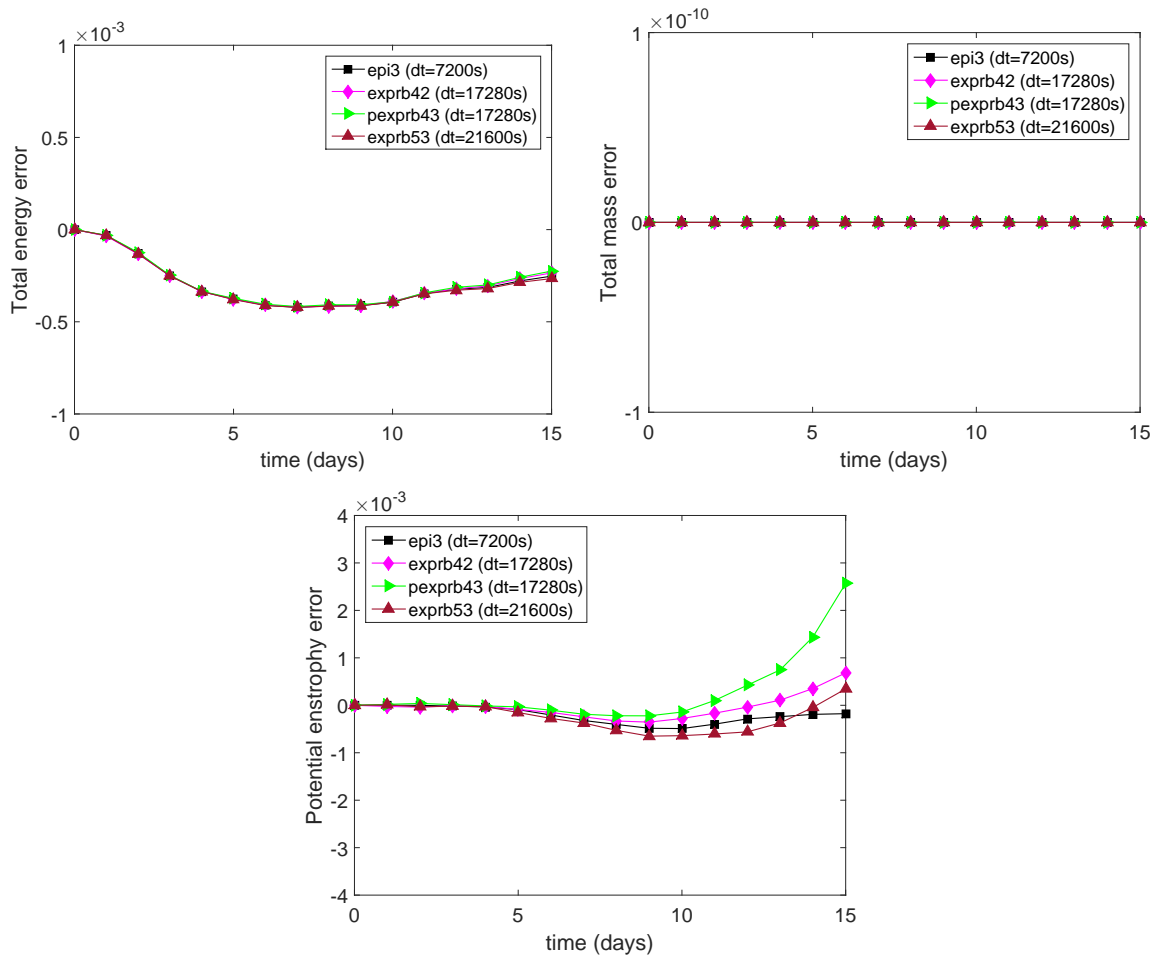
We finally consider the conservation properties of these methods on the Rossby-Haurwitz test, focusing on total mass, total energy and potential enstrophy:

$$\text{Mass} = h, \quad \text{Energy} = gh + \frac{|\mathbf{u}|^2}{2}, \quad \text{Potential Enstrophy} = \frac{(\zeta + f)^2}{2h}.$$

In [12] it was shown that the `epi3` method achieves essentially-perfect conservation of mass, and conserves both energy and enstrophy to within 0.1%, in runs over 15 simulated

days with time steps of size 2h. This behavior is reproduced in Figure 5.5, which shows the same behavior for the `exprb42` and `pexprb43` methods using time steps of size 4.8h, and the `exprb53` method using 6h time steps. We note that these plots show the “normalized” conservation errors, e.g. the normalized error in conservation of mass is computed as  $(\text{Mass}(t) - \text{Mass}(0)) / \text{Mass}(0)$ .

Figure 5.5: The normalized conservation errors for total mass, energy and potential enstrophy for the Rossby-Haurwitz test.



### 5.3 The isolated mountain case

We move to the isolated mountain test case from [46], that introduces flows with a complex vorticity pattern due to perturbation of the flow around an obstacle. We use an identical setup as in [12] for this problem.

We present an identical set of error-related plots and tables as with the Rossby-

Haurwitz test problem:

- Figure 5.6 plots the convergence of each method (similar to Figure 5.2),
- Table 5.3 shows the step sizes required for each method to obtain desired accuracies after one simulated day (similar to Table 5.1),
- Figure 5.7 plots the efficiency of each method (similar to Figure 5.3),
- Figure 5.8 plots the time history of the error over 15 simulated days for each method (similar to Figure 5.4),
- Table 5.4 shows the speedup factors for the proposed methods in comparison with `epi3` (similar to Table 5.2).

Again, to compute solution error in this problem we compare against a high-accuracy reference solution, computed using the `pexprb43` method with a small time step size of 10 seconds. We then compute the  $l_\infty$  error in the height field by comparing other solutions against this reference.

In Figure 5.6 we plot the convergence of each method on the mountain problem after both 1 and 10 simulated days. Two items are particularly interesting. First, the convergence curves for the proposed methods are shifted significantly to the right of the `epi3` curve, indicating that the new methods are much more accurate for a given time step size on this problem. Second, in the 10-day results, both the `epi3` and `pexprb43` methods experience a slight deterioration in convergence at their smallest step sizes.

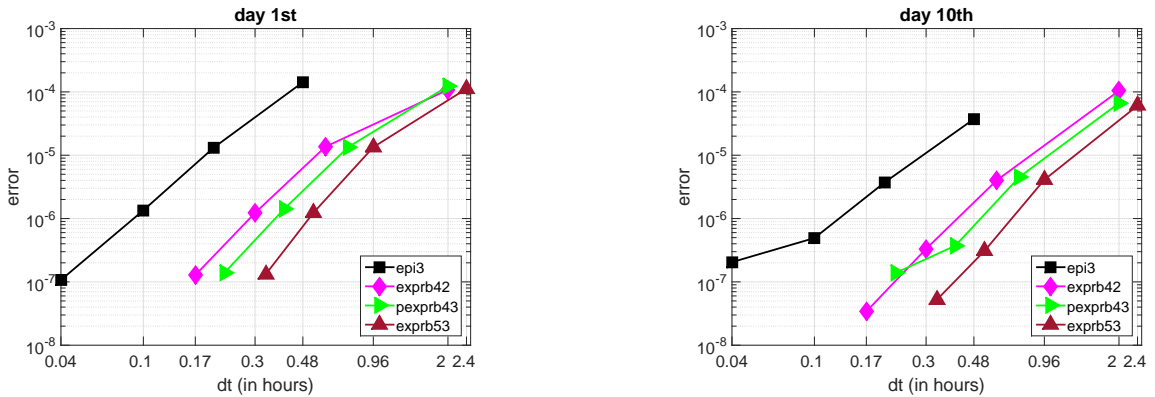


Figure 5.6: Convergence plots for the mountain test. We plot  $l_\infty$  error in the height field as a function of time step size after 1 simulated day (left) and 10 simulated days (right).

Based on these results, we selected a set of time step sizes for each method so that it could obtain accuracies approximately equal to  $10^{-4}$ ,  $10^{-5}$ ,  $10^{-6}$  and  $10^{-7}$  after one simulated day. These values are shown in the following Table 5.3. We note that these

time step sizes are significantly smaller than those for the Rossby-Haurwitz test, due to the increased difficulty with simulation of flow past an obstacle. However, similarly to Table 5.1 we note the trend toward larger step size ratios at tighter accuracies and as method order increases. We also note that here, the smallest time step ratio between `epi3` and the proposed methods is a factor of 3, and the largest is a factor of 7.5, indicating that the proposed methods should show even better efficiency improvements for this problem than the Rossby-Haurwitz test.

Table 5.3: The time step sizes in seconds used for each method to obtain desired accuracies after one simulated day on the mountain test. In parenthesis, we include the normalized step sizes as compared with `epi3` (i.e. we divide by the `epi3` step size at each accuracy).

Method	Accuracy							
	$10^{-4}$		$10^{-5}$		$10^{-6}$		$10^{-7}$	
<code>epi3</code>	1728		720		360		160	
<code>exprb42</code>	7200	(4.17)	2160	(3)	1080	(3)	600	(3.75)
<code>pexprb43</code>	7200	(4.17)	2700	(3.75)	1440	(4)	800	(4.95)
<code>exprb53</code>	8640	(5)	3456	(4.8)	1920	(5.33)	1200	(7.5)

Using these step sizes, we again plot the efficiency of each method in Figure 5.7. As anticipated, the proposed methods are now considerably more efficient than `epi3`; in fact `epi3` is now only more efficient than one method (`exprb53`) at only the loosest tolerance ( $10^{-4}$ ). We again note that at one simulated day, the fifth order method is only competitive at accuracies below  $10^{-7}$ , however at ten simulated days it is now the most efficient method for accuracies below  $10^{-6}$ .

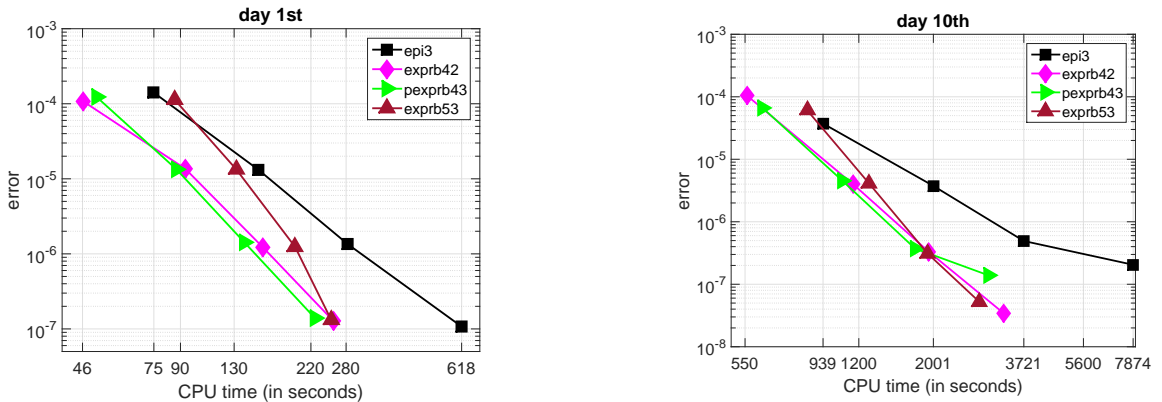


Figure 5.7: Efficiency plots for the mountain test. We plot the  $l_\infty$  error in the height field as a function of CPU time for a variety of time step sizes. Results with one simulated day are on the left, and with 10 simulated days are on the right.

Using the time step sizes from Table 5.3, we again plot the time history of the computed error in each method over fifteen simulated days in Figure 5.8. We note that at the smallest accuracy, the artifact noted earlier in Figure 5.6 has more context – the increase in error at these runs for the `epi3` and `pexprb43` methods at the smallest step size begins at day 5, and progressively increases for the remainder of the run, while the accumulated error for `exprb42` and `exprb53` do not experience a significant increase in error over the full 15-day simulation. That said, all methods show stability at each of these step sizes, even for this more challenging test.

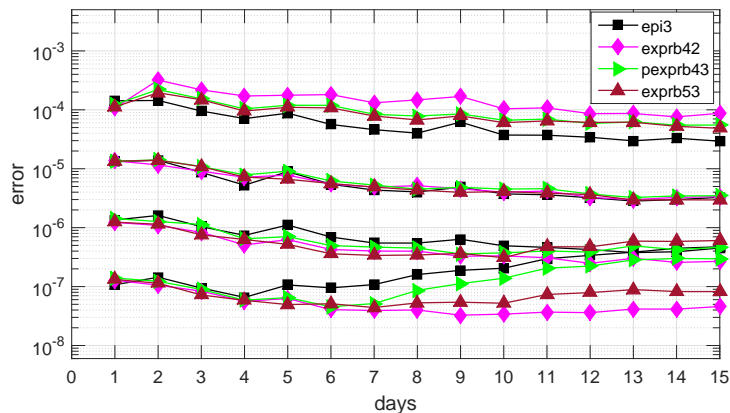


Figure 5.8: Time history of error for the mountain test. We plot the  $l_\infty$  error in the height field over 15 simulated days, using a variety of time step sizes.

We again provide in Table 5.4 a precise comparison of the efficiency for each method at these accuracy levels, produced using the results from 10 simulated days above. As anticipated from Figure 5.7, all of the proposed higher-order methods are more efficient than the `epi3` method, at all accuracies tested. This efficiency gap increases as more accuracy is required, with the higher-order methods uniformly operating over twice as fast as `epi3` for the tightest investigated accuracy of  $10^{-7}$ .

Table 5.4: Speedup factor for the proposed methods in comparison with `epi3` for ten simulated days of the mountain test. Time steps are chosen according to Table 5.3.

Speedup	Accuracy			
	$10^{-4}$	$10^{-5}$	$10^{-6}$	$10^{-7}$
$\text{cpu}_{\text{epi3}}/\text{cpu}_{\text{exprb42}}$	1.68	1.74	1.92	2.42
$\text{cpu}_{\text{epi3}}/\text{cpu}_{\text{pexprb43}}$	1.51	1.87	2.10	2.69
$\text{cpu}_{\text{epi3}}/\text{cpu}_{\text{exprb53}}$	1.11	1.55	1.93	2.87

## 5.4 The unstable jet case

Similarly to [12], our last and most challenging test problem is the unstable jet proposed by Galewsky and collaborators in 2004 [11]. This problem generates vorticity filaments, causing the vorticity gradients to grow exponentially in time, with a corresponding exponential decay in the spatial scale required to resolve such filaments. We counter the introduction of such small-scale features below the spatial resolution of the mesh through a slight increase in our dissipation parameter to  $\gamma_h = 1.25 \times 10^{-2}$ ; the same value as was used in [9].

It was shown in [12] that since exponential integration methods solve the linear portion of the model analytically, they can successfully resolve the highly-curved flow field in this test using much longer time steps than would be otherwise required (e.g. 2 hours for `epi3` versus 30 seconds for the Robert-Asselin-filtered semi-implicit leapfrog scheme in [11]).

For this problem, we again compare accuracy and efficiency results for both `epi3` and our proposed higher-order methods, `exprb42`, `pexprb43` and `exprb53`. In Figure 5.9 we show convergence results. Of note here is that the accuracy gap between `epi3` is larger after 1 simulated day than after 10 simulated days, although the higher-order methods can still compute comparably-accurate solutions using *much* larger time step sizes.

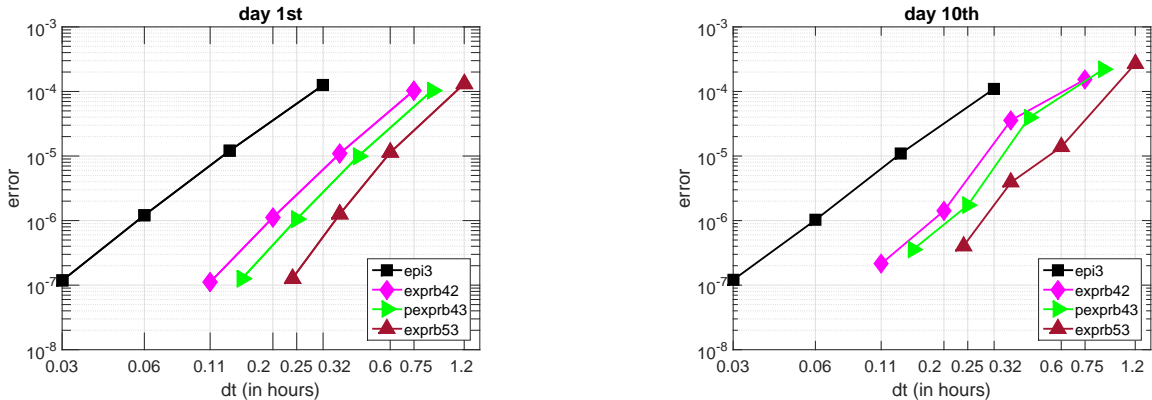


Figure 5.9: Convergence plots for the unstable jet test. We plot  $l_\infty$  error in the height field as a function of time step size after 1 simulated day (left) and 10 simulated days (right).

As with our previous test problems, using the 1-day results from Figure 5.9 we identified step sizes for each method that resulted in accuracies approximately equal to  $10^{-4}$ ,  $10^{-5}$ ,  $10^{-6}$  and  $10^{-7}$ . Table 5.5 contains these values, as well as the ratios of each when compared to the `epi3` method at the same accuracy. Continuing the trend shown in the previous tests, that as the problems increased in difficulty the higher-order methods promise enhanced efficiency over `epi3`, we note the maximum step size ratio of 8.64, again indicating strong potential benefit in using higher order methods as accuracy requirements

tighten.

Table 5.5: The time step sizes in seconds used for each method to obtain desired accuracies after one simulated day on the unstable jet test. In parenthesis, we include the normalized step sizes as compared with `epi3` (i.e. we divide by the `epi3` step size at each accuracy).

Method	Accuracy							
	$10^{-4}$		$10^{-5}$		$10^{-6}$		$10^{-7}$	
<code>epi3</code>	1152		480		216		100	
<code>exprb42</code>	2700	(2.34)	1350	(2.81)	720	(3.33)	400	(4)
<code>pexprb43</code>	3200	(2.78)	1600	(3.33)	900	(4.17)	540	(5.4)
<code>exprb53</code>	4320	(3.75)	2160	(4.5)	1350	(6.25)	864	(8.64)

This is again confirmed in the efficiency plots shown in Figure 5.10, where for one simulated day all of the proposed methods are more efficient than `epi3` at all accuracies, and for ten simulated days the proposed methods beat `epi3` for all accuracies at or below  $10^{-5}$ . We also note that for the unstable jet test, the 5th-order `exprb53` is competitive with the 4th-order `exprb42` and `pexprb43` methods for accuracies at or below  $10^{-6}$  (1 day) and  $10^{-5}$  (10 days).

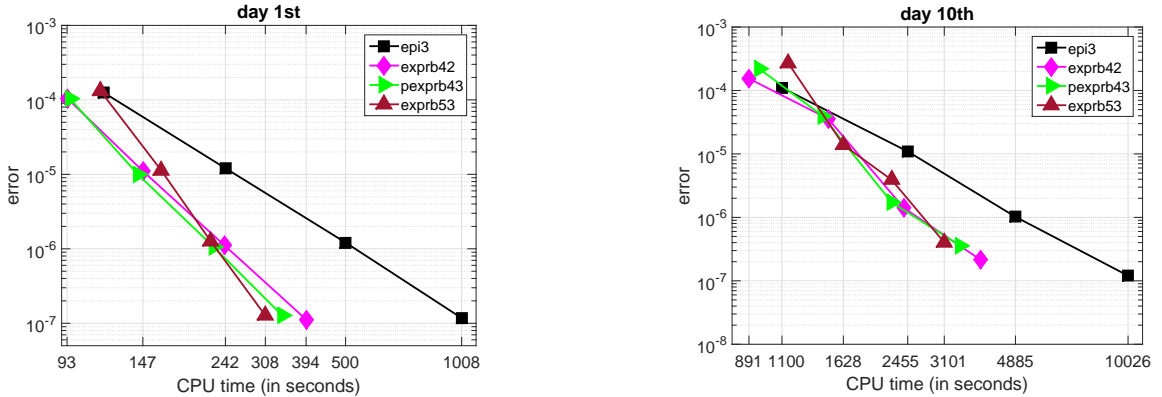


Figure 5.10: Efficiency plots for the unstable jet test. We plot the  $l_\infty$  error in the height field as a function of CPU time for a variety of time step sizes. Results with one simulated day are on the left, and with 10 simulated days are on the right.

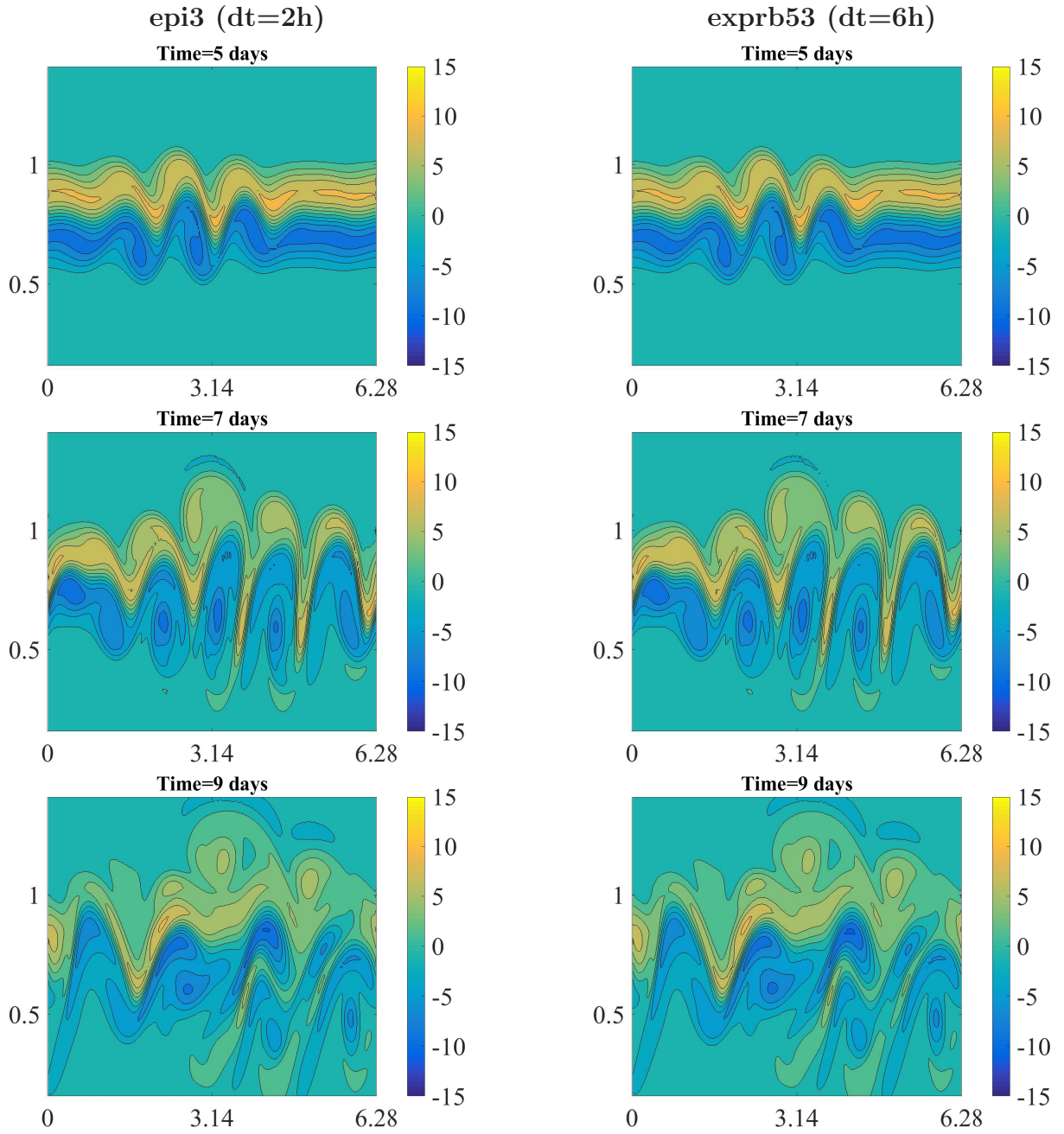
Comparing these CPU times more directly, in Table 5.6 we provide speedup factors for each method as compared with `epi3`, for each of the investigated accuracy values. We again note that at all accuracies the proposed methods are faster than `epi3`, with increasing speedups as the desired solution accuracy improves, to the point that `exprb53` is over three times faster than `epi3` at the tightest investigated accuracy of  $10^{-7}$ .

Table 5.6: Speedup factor for the proposed methods in comparison with `epi3` for one simulated day of the unstable jet test. Time steps are chosen according to Table 5.5.

Speedup	Accuracy			
	$10^{-4}$	$10^{-5}$	$10^{-6}$	$10^{-7}$
<code>cpu<sub>epi3</sub>/cpu<sub>exprb42</sub></code>	1.24	1.65	2.08	2.55
<code>cpu<sub>epi3</sub>/cpu<sub>pexprb43</sub></code>	1.22	1.70	2.22	2.95
<code>cpu<sub>epi3</sub>/cpu<sub>exprb53</sub></code>	1.02	1.47	2.26	3.27

We conclude these results by providing contours of the vorticity field for the unstable jet test in Figure 5.11. Here we compare `epi3` against `exprb53`, where the former uses time steps of size 2 hours, and the latter of size 6 hours. These plots demonstrate qualitative agreement between these two methods (and in turn the results from [11]). We note that the results for `exprb42` and `pexprb43` with time steps of 4h are essentially identical, and are therefore omitted.

Figure 5.11: The vorticity field (scaled by  $10^5$ ) for the unstable jet test.



## 6 Conclusions and Future Work

The shallow water equations posed a significant challenge for early explicit time integration methods, because the CFL criterion resulting from the stiff gravity waves allowed only very short time steps. This situation improved with the introduction of semi-implicit schemes, allowing a sixfold increase in time step size. Subsequently, progress was advanced further by early exponential schemes that could capture the oscillatory term analytically. The resulting increase in time step was indeed impressive, allowing a stable, accurate and efficient integration of the shallow water equations with time steps on the order of  $10^4$  sec on a mesh with horizontal resolution of 100 km (corresponding to a Courant number on the order of 30). Initial publications in this area addressed the description of the method in the meteorological context [9] and the efficiency issues [12]. In this study, we continue this effort through formulation of higher order schemes that approximate the nonlinear part of the problem with increased accuracy. This property is absolutely crucial in order to make the integrations with long time steps not just stable but also meaningful.

We provide a detailed summary of both the accuracy and the efficiency of these methods in Section 5, indicating that the high order schemes offer a significant advantage over the methods considered in the initial tests of exponential schemes in meteorological models, particularly as increased solution accuracy is needed. Specifically, the higher-order methods were competitive, or faster than, `epi3` on all test problems when requiring accuracies at or below  $10^{-5}$ . However, when requiring an accuracy of  $10^{-7}$  the higher-order methods enabled steps from 3.6 to 8.64 times larger than `epi3` on all test problems.

Furthermore, the efficiency improvements resulting from higher-order exponential Rosenbrock methods grew markedly stronger as these test problems increased in nonlinearity. For the relatively simple flows exhibited in the Lauter test in Section 5.1, the accuracy needed to be  $10^{-5}$  or tighter to benefit from these higher-order methods, whereas for the turbulent flows exhibited in the unstable jet test in Section 5.4 the higher-order methods were more efficient than `epi3` at all tested accuracy requirements. These results indicate that the increased resolution of the nonlinear term by the exponential Rosenbrock methods becomes more critical as flows progress into the nonlinear regime.

One question to be addressed in future research is whether these benefits can translate to the compressible Euler equations, which form a fundamental element of current meteorological models. Preliminary experiments in this direction are positive. Even with the second order EPI2 scheme it was possible to perform an integration of convective bubbles, reported in [40], on a grid with resolution of 10 m and time step of 5 sec. The corresponding Courant number with respect to the acoustic waves was on the order of 150. In our future work, we will perform systematic tests using our exponential Rosenbrock methods on this application. In addition, we will investigate the role of sources and sinks related to condensation.

We will further explore the benefit of exponential Rosenbrock methods for atmospheric chemistry, consisting of a large number of coupled advection–diffusion equations with stiff

reaction terms, that still awaits an ideal time integration algorithm. The ultimate goal is to combine, without operator splitting, calculations of the dynamical and physical processes as well as chemistry in a single stable and accurate computational framework.

## Acknowledgements

The numerical results were performed on the *Maneframe2* cluster at Southern Methodist University's Center for Scientific Computation.

## References

- [1] A. H. AL-MOHY AND N. J. HIGHAM, *Computing the action of the matrix exponential, with an application to exponential integrators*, SIAM J. Sci. Comput., 33 (2011), pp. 488–511.
- [2] R. ARCHIBALD, K. J. EVANS, J. DRAKE, AND J. B. W. III, *Multiwavelet discontinuous Galerkin - accelerated exact linear part (ELP) method for the shallow-water equations on the cubed sphere*, Month. Weath. Rev., 139 (2011), pp. 457–473.
- [3] U. M. ASCHER, S. J. RUUTH, AND B. T. WETTON, *Implicit-explicit methods for time-dependent partial differential equations*, SIAM J. Numer. Anal., 32 (1995), pp. 797–823.
- [4] G. BEYLKIN, J. M. KEISER, AND L. VOZOVoi, *A new class of time discretization schemes for the solution of nonlinear PDEs*, J. Comput. Phys., 147 (1998), pp. 362–387.
- [5] G. BISPEN, *IMEX finite volume methods for the shallow water equations*, PhD thesis, Universitätsbibliothek Mainz, 2015.
- [6] M. CALIARI, P. KANDOLF, A. OSTERMANN, AND S. RAINER, *The leja method revisited: Backward error analysis for the matrix exponential*, SIAM J. Sci. Comp., 38 (2016), pp. A1639–A1661.
- [7] J. CERTAINE, *The solution of ordinary differential equations with large time constants*, Math. Meth. for Digit. Comp., (1960), pp. 128–132.
- [8] C. CLANCY AND J. PUDYKIEWICZ, *A class of semi-implicit predictor-corrector schemes for the time integration of atmospheric models*, J. Comput. Phys., 250 (2013), pp. 665–684.
- [9] C. CLANCY AND J. PUDYKIEWICZ, *On the use of exponential time integration methods in atmospheric models*, Tellus A, 65 (2013).

- [10] S. M. COX AND P. C. MATTHEWS, *Exponential time differencing for stiff systems*, J. Comput. Phys., 176 (2002), pp. 430–455.
- [11] J. GALEWSKY, R. K. SCOTT, AND L. M. POLVANI, *An initial–value problem for testing numerical models of the global shallow–water equations*, Tellus, 56A (2004), pp. 429–440.
- [12] S. GAUDREULT AND J. PUDYKIEWICZ, *An efficient exponential time integration method for the numerical solution of the shallow water equations on the sphere*, J. Comput. Phys., 322 (2016), pp. 827–848.
- [13] E. HAIRER AND G. WANNER, *Solving Ordinary Differential Equations II: Stiff and Differential-Algebraic Problems*, Springer, New York, 1996.
- [14] M. HOCHBRUCK AND C. LUBICH, *On Krylov subspace approximations to the matrix exponential operator*, SIAM J. Numer. Anal., 34 (1997), pp. 1911–1925.
- [15] M. HOCHBRUCK, C. LUBICH, AND H. SELHOFER, *Exponential integrators for large systems of differential equations*, SIAM J. Sci. Comput., 19 (1998), pp. 1552–1574.
- [16] M. HOCHBRUCK AND A. OSTERMANN, *Explicit exponential Runge–Kutta methods for semilinear parabolic problems*, SIAM J. Numer. Anal., 43 (2005), pp. 1069–1090.
- [17] M. HOCHBRUCK AND A. OSTERMANN, *Explicit integrators of Rosenbrock-type*, Oberwolfach Reports 3, 3 (2006), pp. 1107–1110.
- [18] M. HOCHBRUCK AND A. OSTERMANN, *Exponential integrators*, Acta Numerica, 19 (2010), pp. 209–286.
- [19] M. HOCHBRUCK AND A. OSTERMANN, *Exponential multistep methods of adams-type*, BIT, 51 (2011), pp. 889–908.
- [20] M. HOCHBRUCK, A. OSTERMANN, AND J. SCHWEITZER, *Exponential rosenbrock-type methods*, SIAM J. Numer. Anal., 47 (2009), pp. 786–803.
- [21] S. K. KAR, *A semi-implicit Runge–Kutta time-difference scheme for the two-dimensional shallow-water equations*, Monthly Weather Review, 134 (2006), pp. 2916–2926.
- [22] A. KOSKELA, *Approximating the matrix exponential of an advection-diffusion operator using the incomplete orthogonalization method*, Numerical Mathematics and Advanced Applications - ENUMATH 2013, (2015), pp. 345–353.
- [23] A. KOSKELA AND A. OSTERMANN, *Exponential Taylor methods: Analysis and implementation*, Comp. Math. with Appl., 65 (2013), pp. 487–499.

- [24] M. LÄUTER, D. HANDORF, AND K. DETHLOFF, *Unsteady analytical solutions of the spherical shallow water equations*, J. Comput. Phys., 210 (2005), pp. 535–553.
- [25] J. LAWSON, *Generalized Runge-Kutta processes for stable systems with large Lipschitz constants*, SIAM J. Numer. Anal., 4 (1967), pp. 372–380.
- [26] V. T. LUAN, *Fourth-order two-stage explicit exponential integrators for time-dependent PDEs*, Applied Numerical Mathematics, 112 (2017), pp. 91–103.
- [27] V. T. LUAN AND A. OSTERMANN, *Exponential B-series: The stiff case*, SIAM J. Numer. Anal., 51 (2013), pp. 3431–3445.
- [28] V. T. LUAN AND A. OSTERMANN, *Exponential Rosenbrock methods of order five—construction, analysis and numerical comparisons*, J. Comput. Appl. Math., 255 (2014), pp. 417–431.
- [29] V. T. LUAN AND A. OSTERMANN, *Stiff order conditions for exponential Runge–Kutta methods of order five*, in Modeling, Simulation and Optimization of Complex Processes - HPSC 2012, H. B. et al., ed., Springer, 2014, pp. 133–143.
- [30] V. T. LUAN AND A. OSTERMANN, *Parallel exponential Rosenbrock methods*, Comput. Math. Appl., 71 (2016), pp. 1137–1150.
- [31] G. MENGALDO, A. WYSZOGRODZKI, M. DIAMANTAKIS, S.-J. LOCK, F. X. GIRALDO, AND N. P. WEDI, *Current and emerging time-integration strategies in global numerical weather and climate prediction*, Archives of Computational Methods in Engineering, (2018), pp. 1–22.
- [32] J. NIESEN AND W. M. WRIGHT, *Algorithm 919: A Krylov subspace algorithm for evaluating the  $\varphi$ -functions appearing in exponential integrators*, ACM Trans. Math. Soft. (TOMS), 38 (2012), p. 22.
- [33] D. A. POPE, *An exponential method of numerical integration of ordinary differential equations*, Comm. ACM, 6 (1963), pp. 491–493.
- [34] J. PUDYKIEWICZ, *On numerical solution of the shallow water equations with chemical reactions on icosahedral geodesic grid*, J. Comput. Phys., 230 (2011), pp. 1956–1991.
- [35] L. F. RICHARDSON, *Weather prediction by numerical process*, Cambridge University Press, 1922.
- [36] A. ROBERT, *The integration of a spectral model of the atmosphere by the implicit method*, Proc. of WMO/ IUGG Symposium on NWP in Tokyo, (1969), pp. VII–19–VII–24.

- [37] A. ROBERT, *A stable numerical integration scheme for the primitive meteorological equations*, Atmosphere-Ocean, 19 (1981), pp. 35–46.
- [38] A. ROBERT, *A semi-lagrangian and semi-implicit numerical integration scheme for the primitive meteorological equations*, J. Meteor. Soc. Japan, 60 (1982), pp. 319–325.
- [39] A. ROBERT, *Efficient time integration schemes for NWP models*, Journal of the Meteorological Society of Japan. Ser. II, 64A (1986), pp. 211–214.
- [40] A. ROBERT, *Bubble convection experiments with a semi-implicit formulation of the Euler equations*, J. Atmos. Sci., 50 (1993), pp. 1865–1873.
- [41] Y. SAAD, *Variations on arnoldi’s method for computing eigenelements of large unsymmetric matrices*, Linear algebra and its applications, 34 (1980), pp. 269–295.
- [42] M. TANGUAY, A. ROBERT, AND R. LAPRISE, *A semi-implicit semi-lagrangian fully compressible regional forecast model*, Mon. Weather Rev., 118 (1990), pp. 1970–1980.
- [43] M. TOKMAN, *Efficient integration of large stiff systems of ODEs with exponential propagation iterative (EPI) methods*, J. Comput. Phys., 213 (2006), pp. 748–776.
- [44] M. TOKMAN, J. LOFFELD, AND P. TRANQUILLI, *New adaptive exponential propagation iterative methods of Runge–Kutta type*, SIAM J. Sci. Comput., 34 (2012), pp. A2650–A2669.
- [45] J. S. WHITAKER AND S. K. KAR, *Implicit-explicit Runge–Kutta methods for fast-slow wave problems*, Monthly Weather Review, 141 (2013), pp. 3426–3434.
- [46] D. WILLIAMSON, J. DRAKE, J. HACK, AND R. J. P. SWARZTRAUBER, *A standard test set for numerical approximations to the shallow water equations in spherical geometry*, J. Comput. Phys., 102 (1992), pp. 211–224.